Supplementary Materials

Table S1. Cryo-EM data collection, refinement, and validation statistics	
Data collection	
Magnification	130k
Defocus range (μm)	0.8-2.4
Voltage (kV)	300
Microscope	Titan Krios
Camera	Gatan K2 Summit
No. of movie frames	35
Total electron dose (e^{-}/Å^{-2})	50
Pixel size (Å)	1.1
Reconstruction	
Total number of segments extracted	227,444
No. of segments used for final reconstruction	35,719
Resolution (Å)	3.82
Map sharpening B-factor (Å^2)	30
Helical rise (Å)	4.95
Helical twist (°)	-0.64
Atomic model	
Ramachandran plot values	%
Outliers	2.33
Allowed	17.05
Favored	80.62
Rotamer outliers (%)	2.63
MolProbity Score	3.05
Clashscore	32.83
RMS deviations	
Length (Å)	0.008
Angles (°)	2.061
Map model CC (mask)	0.59
Map model CC (volume)	0.60

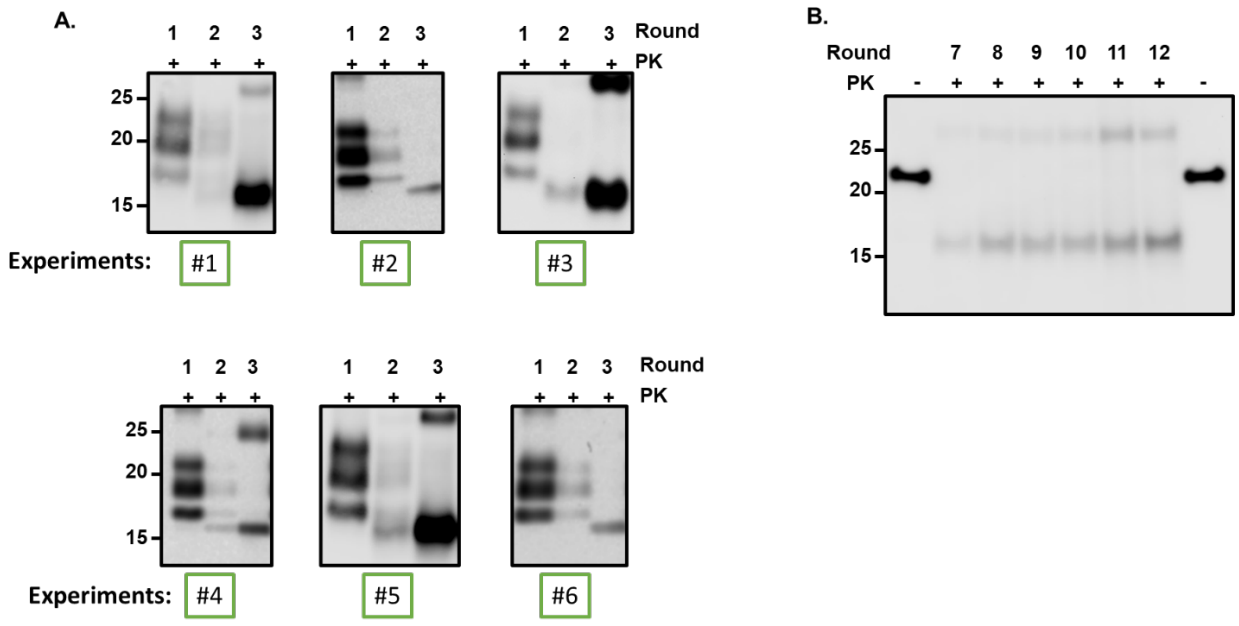

Figure S1. Generation of recPrP^{res} by RML-seeded PMCA. (**A**) Independent experiments showing the generation of additional batches of recPrP^{res} in PMCA reactions seeded with RML prions. PMCA products from rounds 1 to 3 were subjected to PK digestion and immunoblotting. (**B**) PMCA products (first batch) from rounds 7 to 12 were subjected to PK digestion and immunoblotting. The anti-PrP monoclonal antibody 6D11 was used to detect PrP.

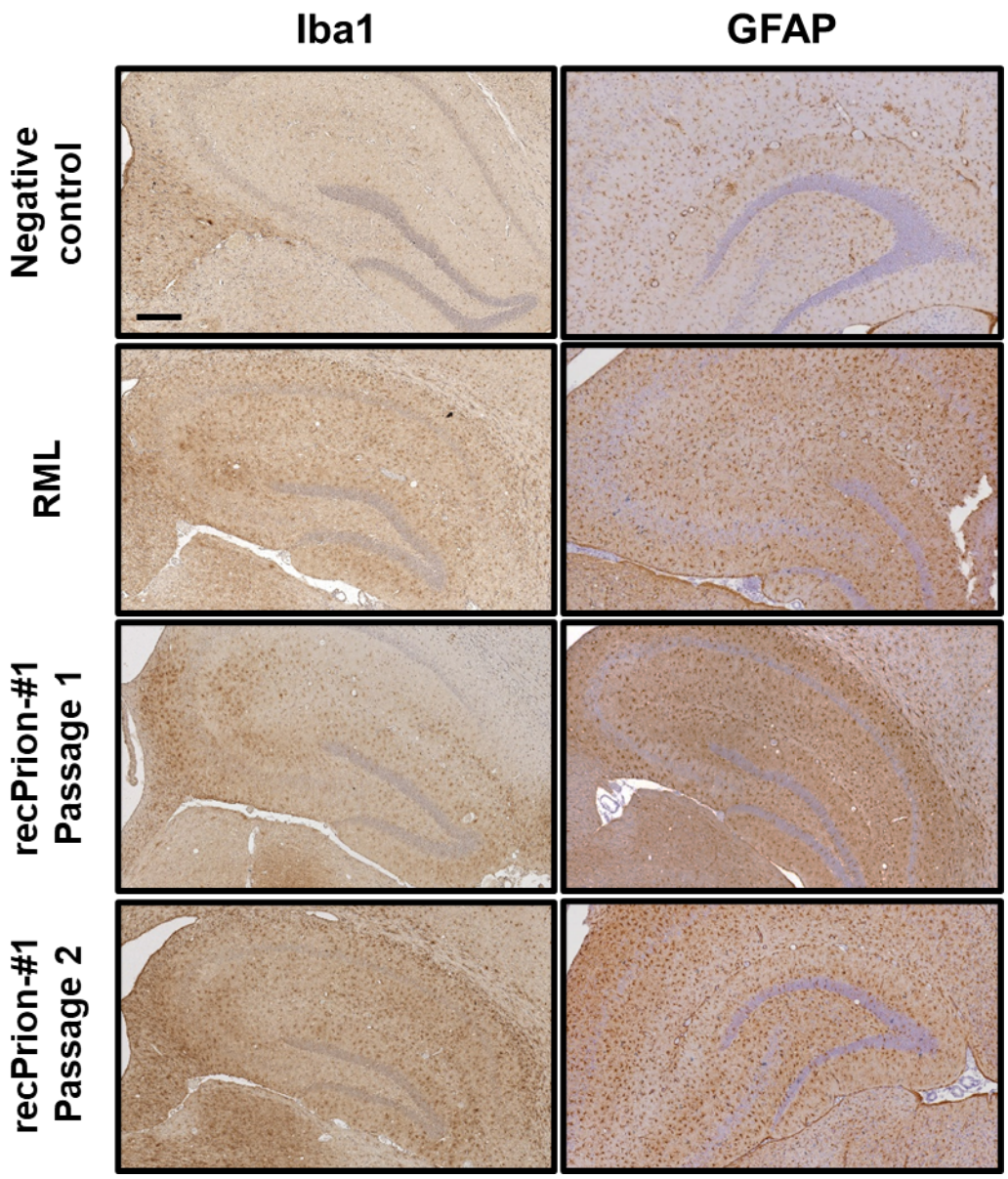

Figure S2. Histological analyses of brain inflammation in mouse brains. Representative images of hippocampal regions from each group show activated microglia, as indicated by anti-Iba1 antibody staining, and reactive astrogliosis, as indicated by anti-GFAP antibody staining. Scale bar: 200 μm.

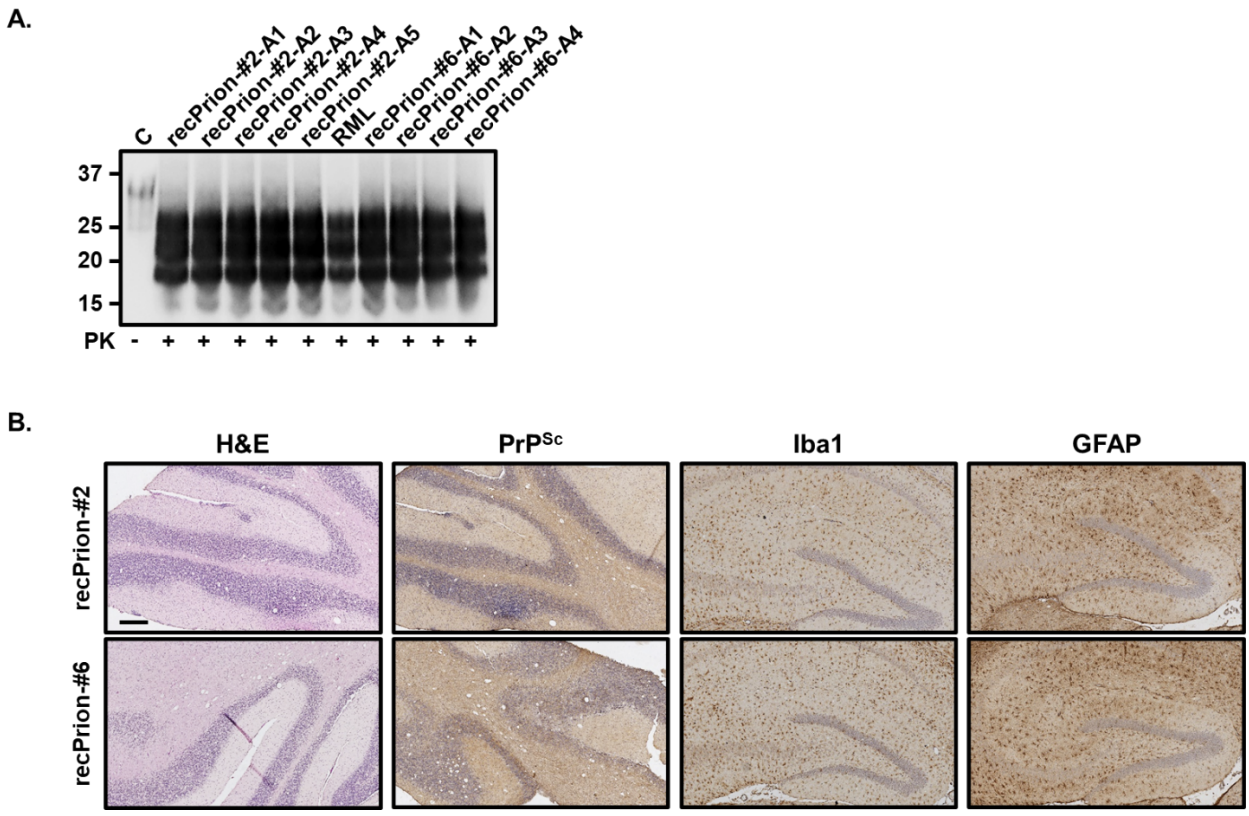

Figure S3. Biochemical and histological analysis of the brain of animals infected with recPrP^{res} generated in independent experiments. (**A**) Immunoblotting analysis of the PK-resistant PrP in brains of five mice from recPrion-#2 and four mice from recPrion-#6 (P1), and one RML-infected mouse. The anti-PrP monoclonal antibody 6D11 was used to detect PrP. (**B**) Histopathological analyses of neurodegeneration in recPrion-infected mice. Representative images of cerebellar regions from each group show vacuolation, as indicated by hematoxylin-eosin staining and PrP^{Sc} deposition, as indicated by anti-PrP staining, and representative images of hippocampal regions from each group show activated microglia, as indicated by anti-Iba1 staining, and reactive astrogliosis, as indicated by anti-GFAP staining. Scale bar: 200 µm.

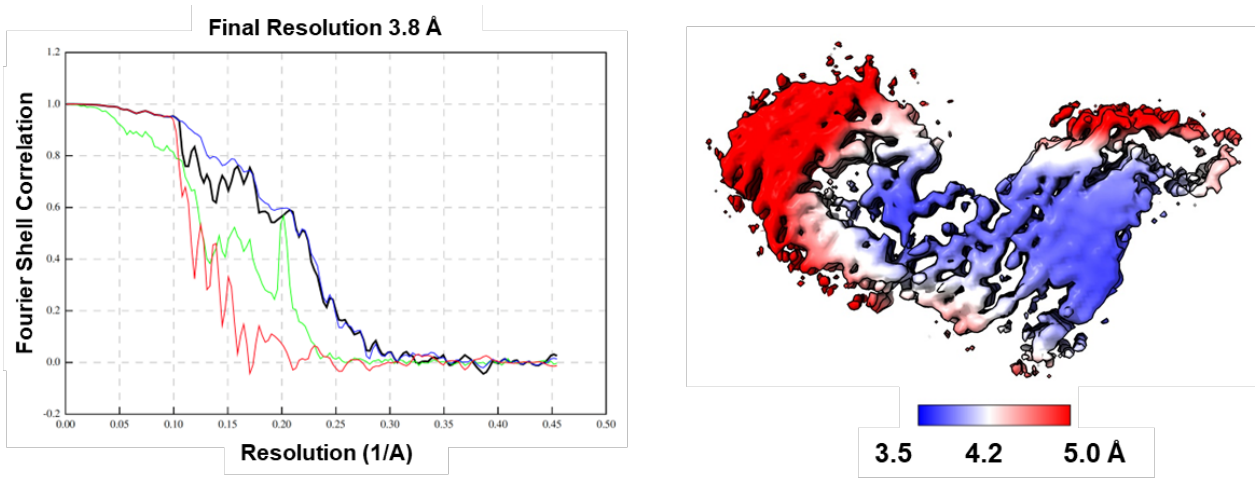

Figure S4. Structural validation for PMCA-propagated recPrP^{res} fibrils. Left panel: Gold-standard Fourier shell correlation (FSC) curve for the final 3D reconstruction, yielding a resolution of 3.8 Å at the FSC = 0.143 criterion. Right panel: Local resolution map of PMCA-propagated recPrP^{res} fibrils. Local resolution was calculated using the RELION post-processed map.

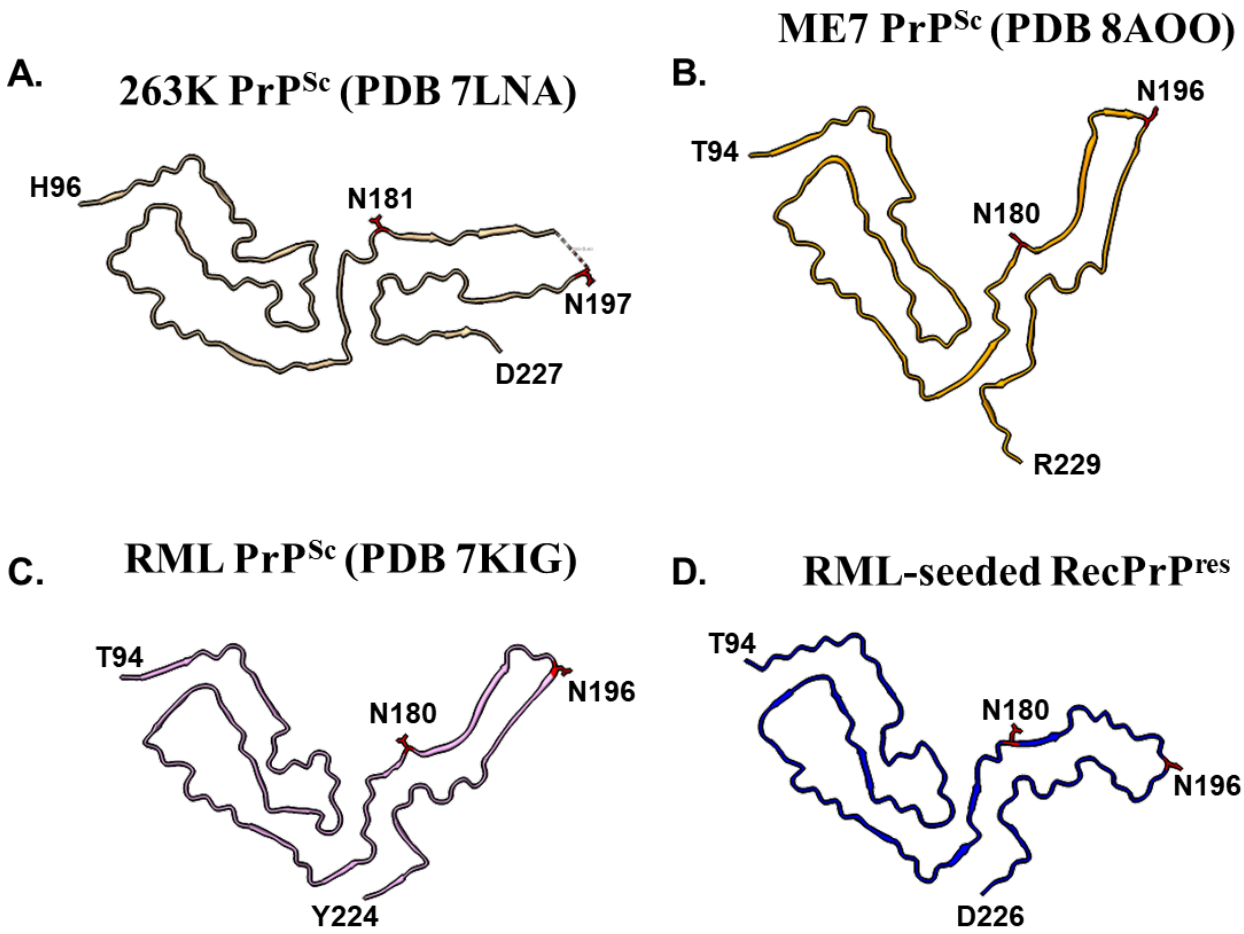

Figure S5. Comparison of published rodent PrP^{Sc} and PMCA-propagated $recPrP^{res}$ structures. (**A**) Ex vivo hamster 263K PrP^{Sc} (PDB 7LNA), (**B**) Ex vivo mouse ME7 PrP^{Sc} (PDB 8AOO), (**C**) Ex vivo mouse RML PrP^{Sc} (PDB 7QIG), (**D**) PMCA-propagated $recPrP^{res}$ fibril. Residues N180/N181 and N196/N197 are highlighted in all models. Across all four structures, the characteristic V-shaped architecture of PrP^{Sc} is preserved. In all fibrils, both N-linked glycosylation sites (N180/N181 and N196/N197) are positioned away from the fibril core and are consistent with solvent accessibility.

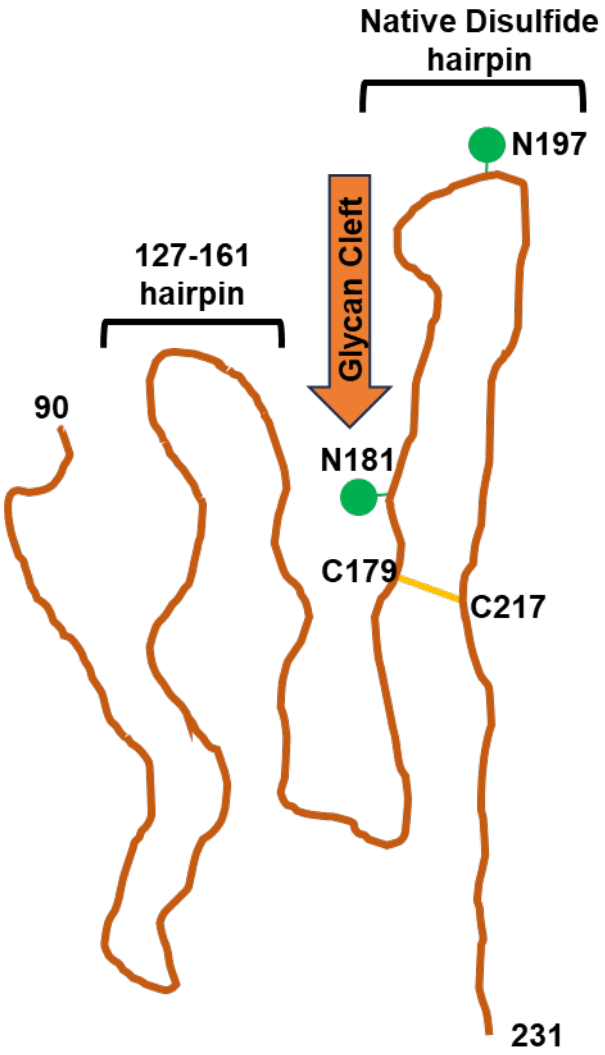

Figure S6. Structural model of RT-QuIC-propagated recPrP fibrils. This schematic model was adapted from Figure 5 of a previously published article (ref [15]).